Journal of Alloys and Compounds 764 (2018) 815–823

Contents lists available at ScienceDirect

Journal of Alloys and Compounds

journal homepage: http://www.elsevier.com/locate/jalcom

Effect of heat treatments on microstructure evolution and grain morphology of alloy 625 with 0.4 wt% boron modification fabricated by laser wire deposition

Y. Tian, N. Chekir, X. Wang, A. Nommeots-Nomm, R. Gauvin, M. Brochu*

Department of Mining and Materials Engineering, McGill University, 3610 University Street, Wong Building, Montreal, Quebec, H3A 0C5, Canada

ARTICLE INFO

Article history:
Received 6 April 2018
Received in revised form
6 June 2018
Accepted 11 June 2018
Available online 15 June 2018

Keywords:
Alloy 625
Laser wire deposition
Microstructure
Grain morphology

ABSTRACT

Alloy 625 modified with 0.4 wt% B was deposited on stainless steel 304 substrate by laser wire deposition. The microstructure was characterized and grain morphology was analyzed in the as-deposited and two post heat-treated conditions. In the as-deposited condition, continuous eutectics were observed to segregate in the inter-dendritic regions. The eutectics mainly consist of Laves phase and small amount of NbC precipitates. It was also found that the solidification features in the layer boundary were coarser than the layer core due to the recalescence mechanism. Small equiaxed grains nucleated in the layer boundary and eliminated the epitaxial growth which is normally formed during the additive manufacturing process. In the two-step aging condition, the eutectics were almost fully dissolved in the layer boundary. This has been associated with the layer boundary's larger elemental diffusion path when compared to the layer core. Partial recrystallization occurred in the layer core and led to nucleation of equiaxed grains. The grain size in both the layer boundary and the layer core coarsened during heat treatment. In the annealed and aged condition, the eutectics observed in the as-deposited condition were fully re-melted, resulting in the formation of large sized M_5B_3 borides during re-solidification. The fraction of borides in the layer boundary was lower, with smaller sized precipitates than those in the layer core. Similarly, to the two-step aged condition, partial recrystallization and grain growth developed during annealing and aging treatment.

1. Introduction

Nickel-based superalloys are utilized for high temperature components, such as gas turbine blades and vanes, due to their excellent combination of mechanical properties, oxidation and corrosion resistance in high temperature and aggressive environments [1–3]. Because of the high cost of the parts due to their complex design and expensive raw materials, repairing techniques are usually favored instead of replacement after the occurrence of impacting erosions, fatigue cracks and other defects which develop during service life. Nowadays, laser wire deposition is employed for the repair of damaged gas turbine components. As a layer-by-layer laser additive manufacturing (LAM) technology [4], the laser wire deposition process can re-construct the damaged substrate with little distortion or dilution. It also boasts of a near net shape building process that can produce complicated profiles and dimensions without the need for significant post treatment.

Nickel-based Alloy 625, is one type of solid solution strengthened nickel-based superalloys, its composition includes refractory elements Nb and Mo [2,3,5]. Alloy 625 is usually chosen as a repairing material owing to its good weldability and mechanical properties [6–10]. However, for the repair of components made from precipitation strengthening nickel-based superalloys, the base metal is prone to hot cracking issues during deposition solidification [1,11,12] and strain-age cracking issue during heat treatment (for γ' based nickel based superalloys) [1]. In order to circumvent this problem, Alloy 625 was modified with 0.4 wt% B in order to increase the eutectic volume percent formed at terminal solidification, so that the additional liquid eutectics could backfill any cracks which are formed [13]. The feasibility of adding B into Alloy 625 to increase the eutectic amount has been demonstrated in previous research [14,15], where the eutectic fraction was increased from 2% in conventional Alloy 625 [16] to around 12% in 0.4 wt% B

* Corresponding author.
E-mail address: mathieu.brochu@mcgill.ca (M. Brochu).

https://doi.org/10.1016/j.jallcom.2018.06.106
0925-8388/

modified Alloy 625 during gas tungsten arc deposition. After a high temperature heat treatment [15], the eutectics formed during deposition are re-melted and the coarsened discrete borides are formed. It is postulated that the re-melting of the eutectics could heal any potential strain-age cracks, which may develop, during the heat-treatment stage [17].

In the current research, laser wire deposited samples were made using Alloy 625 with 0.4 wt% B modification. The heat treatment processes that are standard for the repairing of IGT engine components manufactured of IN738 and GTD111 superalloys were conducted [18]. The microstructure evolution and grain morphology development were compared between the as-deposited condition and after two different heat-treated conditions.

2. Experimental procedure

The samples for this research were produced at Liburdi Turbine Service. Laser wire deposition using Liburdi LAWS 1000 system on a stainless steel 304 substrate was conducted using wire manufactured of Alloy 625 with 0.4 wt% B (referred to as 625B) as per pending patent application [19]. The diameter of 625B wire used in the study was about 1.14 mm. The chemical composition of 625B wires was (wt%) 21 Cr, 9 Mo, 3.7 Nb, 1 Co, 0.4 Al, 0.4 Ti, 0.4 B, 0.0 2C and balance Ni. This chemical composition was confirmed by both a Thermo Scientific™ ELEMENT 2™ inductively coupled plasma-mass spectrometry (ICP-MS) and a JEOL 8900 Electron Probe Microanalysis (EPMA) tests.

During the deposition, about ten layers of deposits were constructed on the substrate, with approximately dimensions of 20 mm in height, 3 mm in width, and 50 mm in length. The laser beam power used was 800 W. Argon was employed as a shielding gas during the deposition.

After deposition, one sample was subjected to a standard primary aging at 1120 °C for 2 h followed by a secondary aging at 845 °C for 24 h. Another sample was exposed to a standard annealing stage for 2 h at 1205 °C, followed by the same two-step aging process.

The as-deposited and heat-treated samples were sectioned along the transverse direction, followed by sequential grinding steps up to 800 grit, and standard polishing steps up to 1 μm. The polished samples were electrolytically etched in a solution of 12 ml H_3PO_4 + 40 ml HNO_3 + 48 ml H_2SO_4 at 6 V for 5s in order to characterize the microstructure [20]. The microstructure of the samples was characterized using a Nikon optical light microscope with Clemex Vision System, a SU3500 scanning electron microscope (SEM) equipped with electron dispersive spectrometer (EDS) analysis. Five different regions were chosen in order to measure the dendrite arm spacing and area fractions of secondary phases using ImageJ image analysis software [21], and the average results are presented in this discussion. Based on the similar procedure to measure grain size according to ASTM E112 [22], the dendrite arm spacing was measured manually by dividing the length of a line by the number of dendrites contained within the line. To measure the area fractions of secondary phases, the acquired micrographs were treated to enhance the contrast and better define the boundary between the secondary phases and γ solid solution. This image processing step permitted the proper delineation required for regular image analysis routine using ImageJ. Interaction volumes of 16 μm^3 for EDS were calculated using Monte Carlo simulation from Casino [23]. The grain morphology of the samples was studied using electron backscattered diffraction (EBSD) linked to SU3500

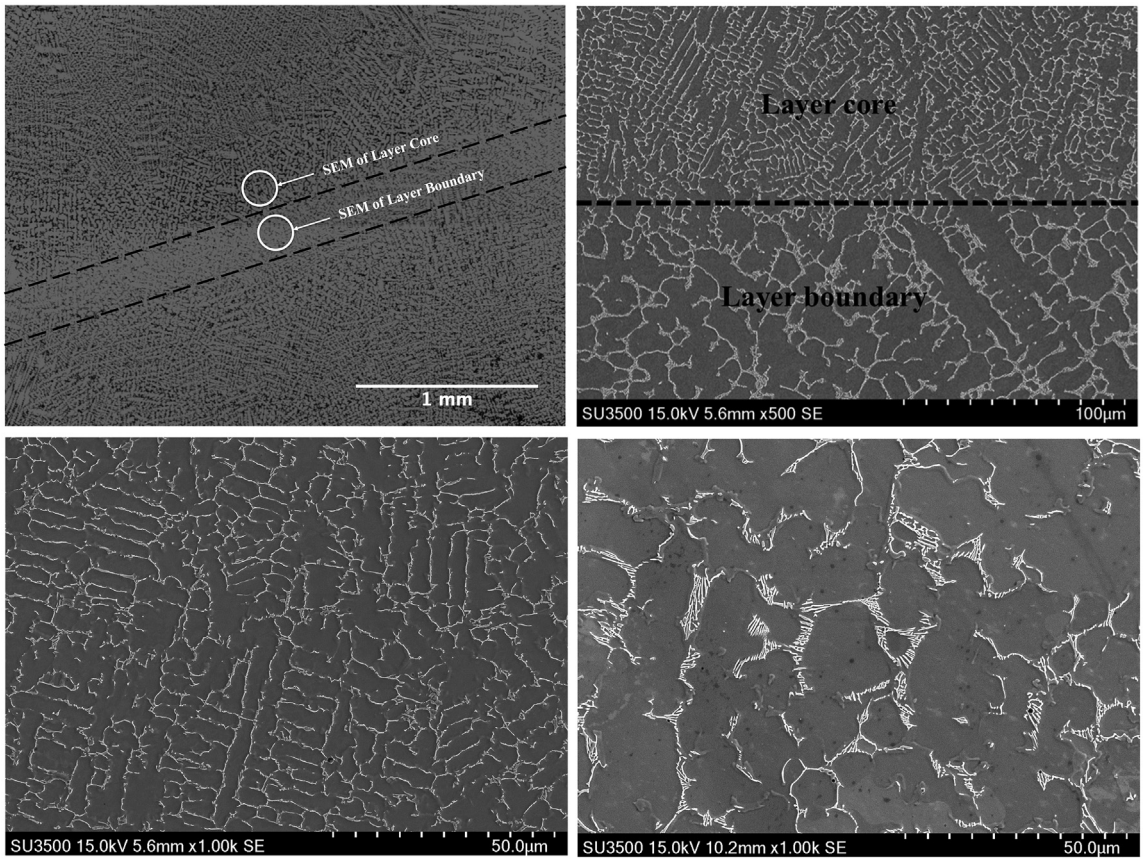

Fig. 1. (a) Optical microscope image of the as-deposited sample showing layer boundary with thickness of around 250 μm. (b). SEM micrograph showing larger feature in the layer boundary than the inner layer region in the as-deposited condition; (c) Higher magnified SEM micrograph of layer core; (d) Higher magnified SEM micrograph of layer boundary.

SEM machine. The samples for EBSD were polished up to 0.05 μm in the colloidal silica suspension. The Aztec data acquisition software employed with the HKL Channel 5 data processing software was used for the EBSD analysis. The analysis of the samples in the bottom part and near the substrate are not discussed in the present work owing to the high influence of the dilution from substrate.

The samples microhardness was measured by a CM-100AT Clark Microhardness Indenter using 200 g load. Five different locations were selected for each condition, and the average results were reported in the discussion.

3. Results and discussion

3.1. As-deposited condition

Fig. 1(a) is a representative optical microscope micrograph of the as-deposited sample. As depicted, a layer boundary with thickness of around 250 μm can be clearly observed between the two

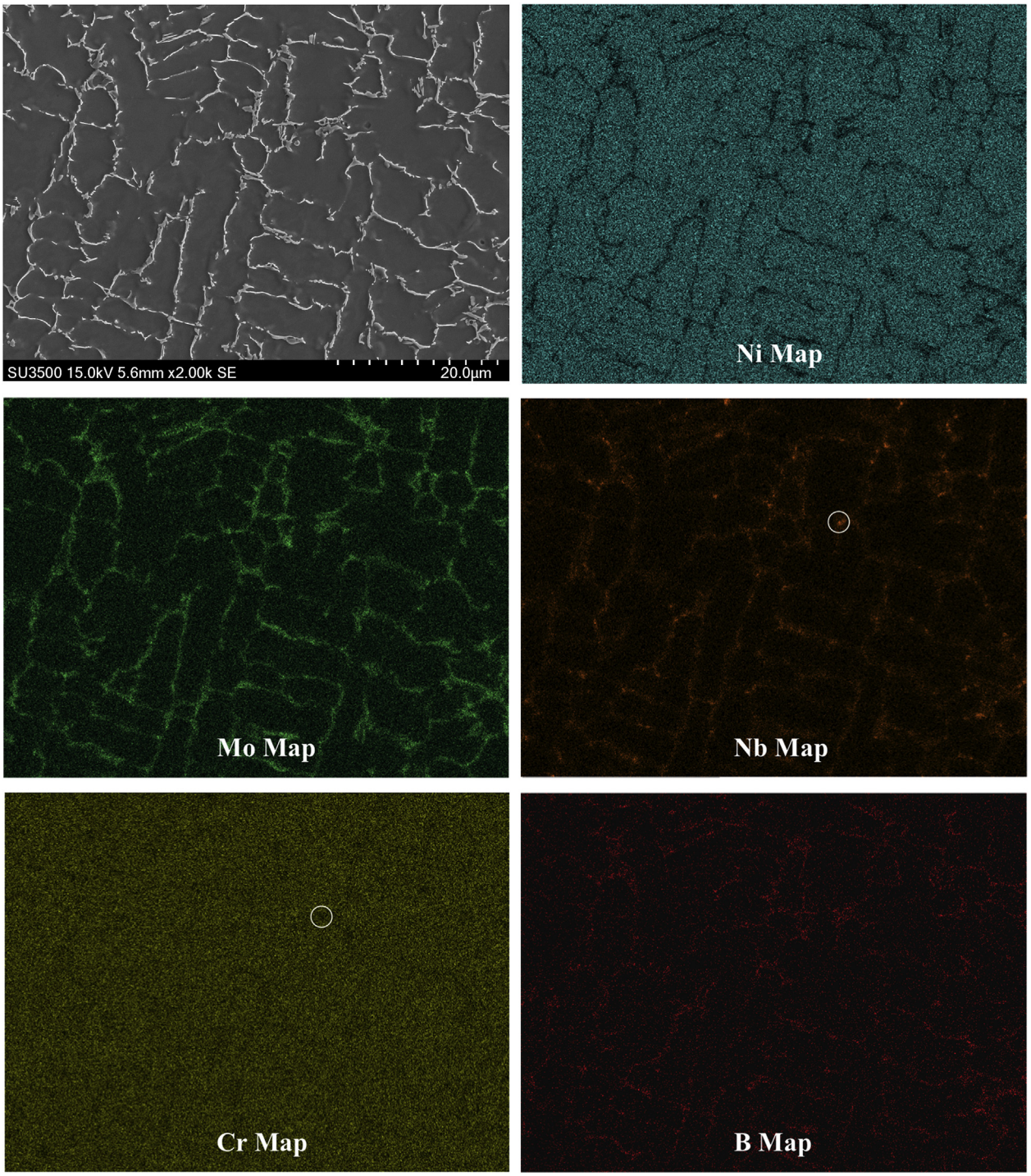

Fig. 2. a). SEM micrograph in the layer core showing continuous eutectic in inter-dendritic regions for the as-deposited condition; EDS maps of (b) Ni map; (c) Mo map; (d) Nb map; (e) Cr map; (f) B map. White circle represents NbC that composed of Nb and Mo, and depleted in Cr.

deposits. The layer boundary was formed due to the re-melting of the previous deposit by the subsequent laser scan. Layer boundary formation is typical during the production of additive manufactured samples produced via layer-by-layer construction [24].

A representative SEM micrograph of the layer core and layer boundary in the as-deposited condition is shown in Fig. 1(b). The higher magnified micrographs for layer core and layer boundary are shown in Fig. 1(c) and (d), respectively. It can be seen from Fig. 1(b)–(d) that both the layer core and layer boundary show a dendritic microstructure, and the continuous eutectics are segregated at the inter-dendritic regions. However, the solidification microstructure at the layer boundary is larger than that of the layer core, with the measured dendrite arm spacing (DAS) for the layer core and layer boundary of $4.8 \pm 0.9\,\mu m$ and $7.2 \pm 1.2\,\mu m$, respectively. This coarsened morphology in the layer boundary is associated with the recalescence phenomena. This occurs when the latent heat flow speed becomes retarded by the formation of primary γ phase at the beginning of solidification. This results in a decreased temperature gradient and consequent cooling rate and leads to the observed larger microstructure. The area fractions of the eutectics in the layer core and layer boundary were measured to be $8.6 \pm 1.3\%$ and $5.4 \pm 1.5\%$, respectively. Both values are significantly higher than 2% of eutectics reported for the conventional Alloy 625 after welding solidification [16]; proving the effectiveness of the B modification in Alloy 625 to increase the eutectic volume percentage during laser wire deposition. This eutectic amount is believed to be sufficient to guarantee crack free build in both the deposits and substrate [20].

EDS maps of the major alloying elements (Ni, Mo, Nb, Cr and B) were acquired to observe the elemental concentration and distribution of the different phases in the layer core in the as-deposited condition. The maps are presented in Fig. 2. As depicted, the γ matrix is enriched with Ni and Cr, the continuous eutectics at the inter-dendritic regions consist mainly of Laves phase which are rich in Nb, Mo and B, and a small portion of NbC that is composed of Nb and Mo, and depleted of Cr (see circles in Fig. 2(d) and (e)). It is known that Laves phase is an intermetallic compound with the X_2Y type structure, where X (including Ni and Cr) is the solid constituent, and Y (including Nb and Mo) is the liquid constituent in conventional Alloy 625 [1]. In the present case, the addition of B as a melting point reduction element, could substitute into the liquid constituent (Y) and lead to an increased amount of Laves eutectics during terminal solidification. The feasibility of elemental substitution in Laves phase by B has been proved in previous research using the density functional theory (DFT) [14]. The EDS maps of the layer boundary are similar to that of the layer core, and the eutectics observed in the layer boundary include predominantly Laves phase with a small amount of NbC.

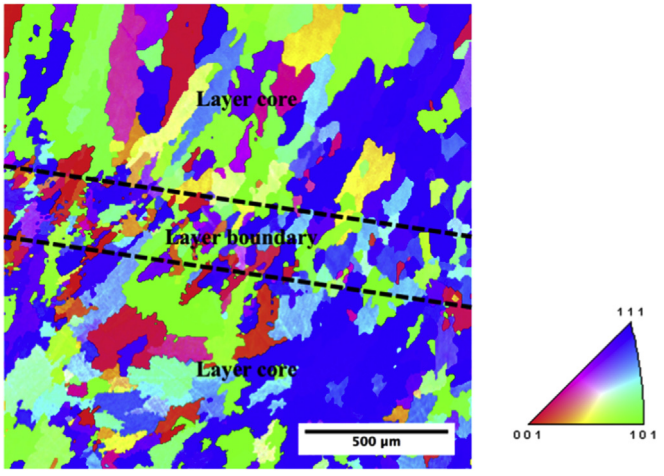

Fig. 3. EBSD map of the as-deposited sample (with colored orientation image map inserted in the right) showing small equiaxed grains in the layer boundary and columnar grains dominating in the layer core.

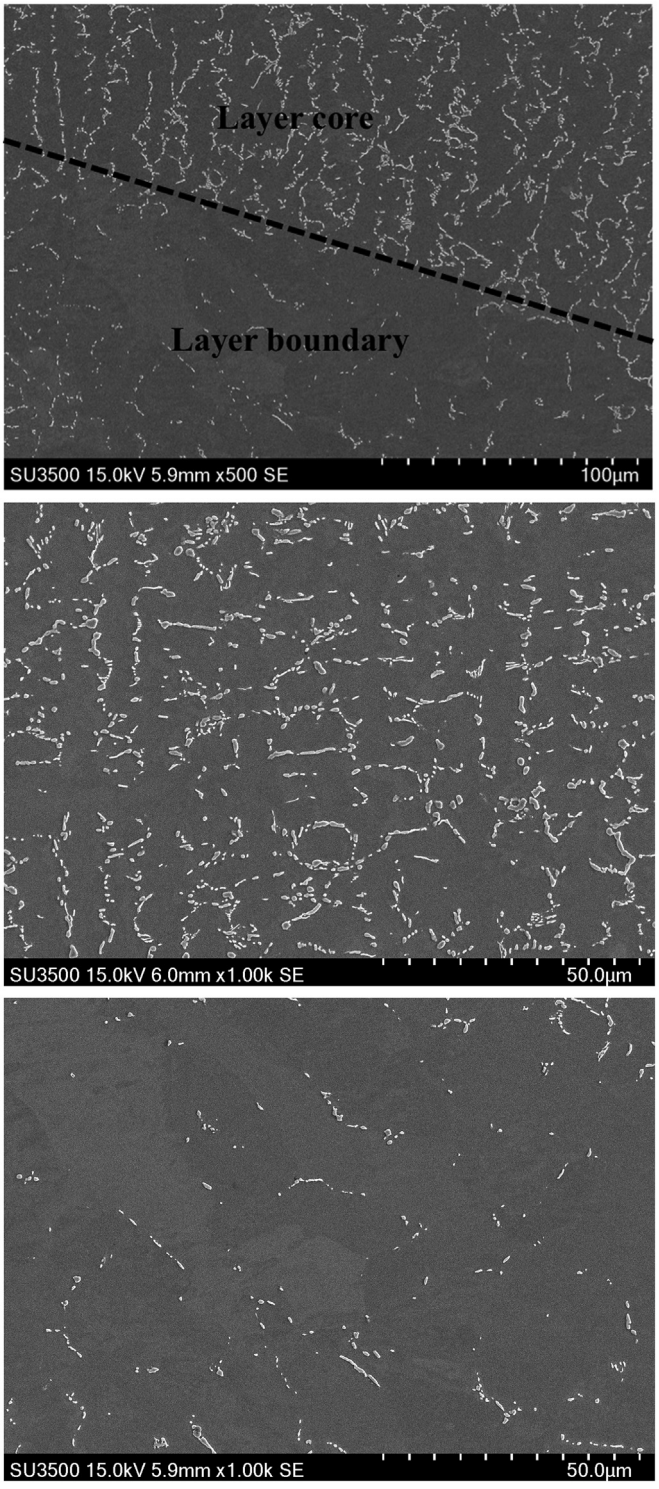

Fig. 4. (a) SEM micrograph showing the transition between layer core and layer boundary in the two-step aged condition; (b) Higher magnified SEM micrograph of layer core; (c) Higher magnified SEM micrograph of layer boundary.

EBSD mapping was used to observe the grain morphology of the as-deposited condition, and the results are presented in Fig. 3. As depicted, small equiaxed γ grains are observed in the layer boundary, while large columnar γ grains with small amount of equiaxed grains are dominant in the layer core. The thickness of the layer boundary was measured to be around 250 μm and was in good agreement with the observation shown in Fig. 1(a). The observed solidification mode, with equiaxed grains in the layer boundary, differed from the epitaxial columnar grain growth which typically occurs along the build direction of conventional Alloy 625 during additive manufacturing [25,26]. It is known that the melting point depressant B can decrease the viscosity of the liquid at the beginning of solidification [27]. This decrease in viscosity reportedly reduces the surface tension and enhances the wettability of

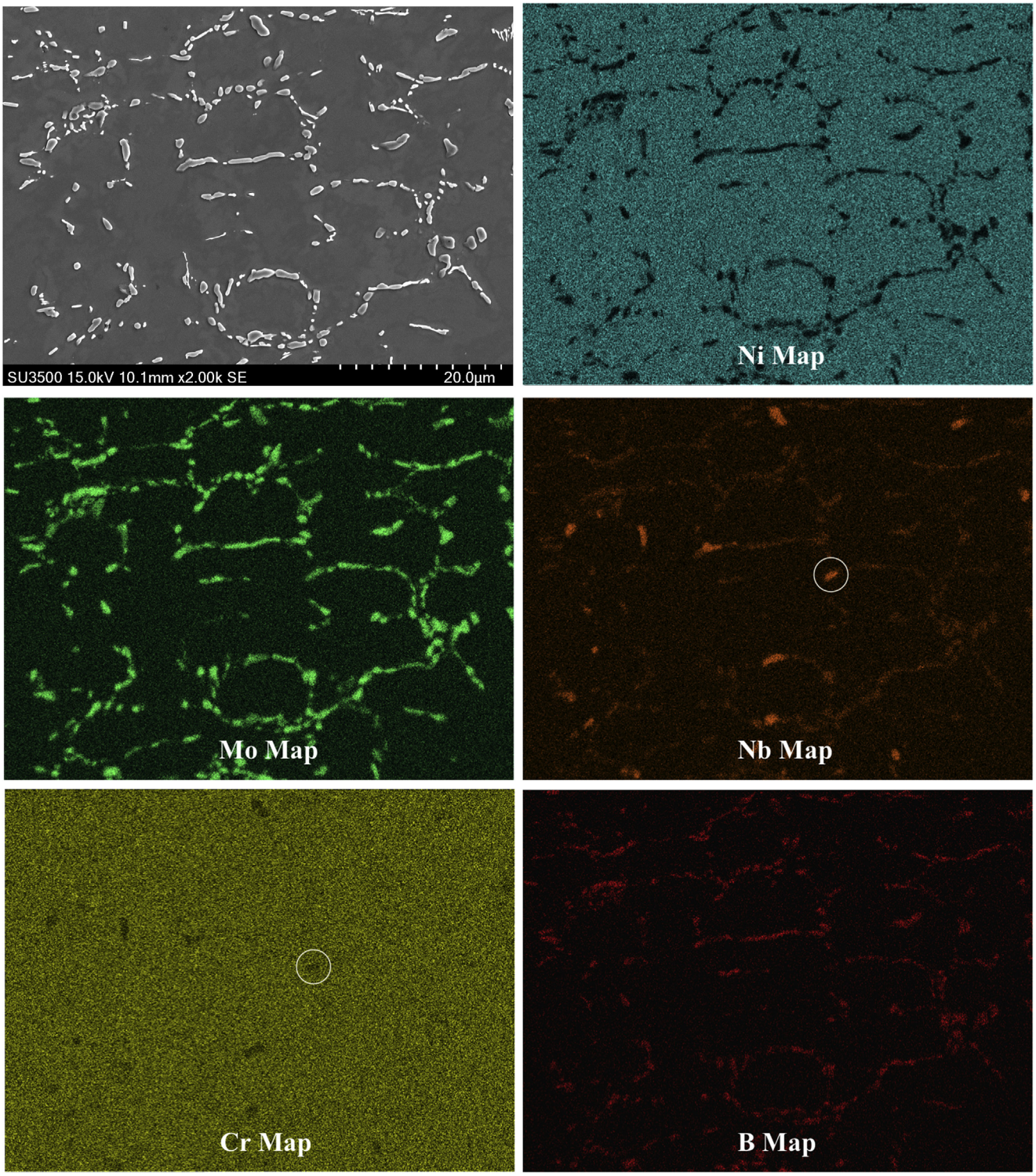

Fig. 5. (a). SEM micrograph in the layer core showing non-continuous eutectic in inter-dendritic regions after aging treatment; EDS maps of (b) Ni map; (c) Mo map; (d) Nb map; (e) Cr map; (f) B map. White circle represents NbC that composed of Nb and Mo, and depleted in Cr.

the system, so that more heterogeneous nucleation events can develop [28]. The increased number of nucleation sites could promote the equiaxed grain nucleation and growth that is observed in the layer boundary [28].

3.2. Two-step aged condition

The SEM micrograph showing the transition between the layer core and the layer boundary after a two-step aging treatment is shown in Fig. 4(a). Higher magnification micrographs for the layer core and the layer boundary are presented in Fig. 4(b) and (c), respectively. As depicted, the layer core had a dendritic microstructure with DAS measured to be 4.9 ± 0.8 μm, which was similar to the as-deposited condition. The area fraction of eutectics in the layer core in the two-step aged condition was 7.8 ± 1.1% and was comparable to the as-deposited condition of 8.6 ± 1.3%. Previous study has shown that the onset temperature for the melting of Laves phase and NbC formed in 625B is 1191.5 °C and 1266.7 °C, respectively [14]. This value is higher than the temperature of the primary aging treatment used within this study of 1120 °C, so that the aging treatment were unable to re-melt the eutectics. However, the continuous eutectics that formed in the as-deposited condition were transformed into non-continuous features in the layer core due to Oswald Ripening occurring during aging. Fig. 4(a) and (c) shows that a high percentage of eutectic were dissolved in the layer boundary compared to the layer core, with the area fraction of remaining eutectics in the layer boundary calculated to be 2.1 ± 1.3%. The dissolution of eutectics in the layer boundary was associated with its larger microstructure, allowing greater diffusion to occur due to the larger elemental diffusion path.

EDS maps of the main alloying elements (Ni, Mo, Nb, Cr and B) were gathered to analyze the potential phase transformation in the layer core during the two-step aging treatment, the results are shown in Fig. 5. Results show that the same phases with similar elemental constitution as in the aged condition was present in the as-deposited condition. In the dendritic cores, the γ matrix was shown to be rich in Ni and Cr. Whereas, in the inter-dendritic regions, the eutectics consisted of mainly Laves phase and a small part of NbC. The Laves phase was enriched with Nb, Mo and B. The NbC composed of Nb and Mo, with depleted Cr concentrations (highlighted in Fig. 5(d) and (e). The size of NbC precipitates are larger than those in the as-deposited condition, as shown from comparison between Figs. 2 and 5. This is due to the coarsening effect which occurs during the aging treatment. The remaining eutectics in the layer boundary also consisted of Laves phase with a few NbC precipitates of similar chemical constitution to the layer core.

EBSD mapping was performed to observe the change in grain morphology after the aging treatment; the result are presented in Fig. 6. As depicted, the grain size in both the layer boundary and the layer core coarsened during the aging treatment (see comparison between Figs. 3 and 6. The layer boundary, as seen previously, was still comprised of equiaxed grains. In the layer core, however, many more equiaxed grains were nucleated in the two-step aged condition than the as-deposited condition. These equiaxed grains were formed due to partial recrystallization occurring during the aging treatment.

3.3. Annealed and aged condition

The SEM micrographs of the layer core and layer boundary after the annealed and aged cycles are shown in Fig. 7(a) and (b), respectively. Fig. 7(a) depicts the discrete borides with an irregular morphology ranging from 0.5 to 5 μm in size developed in the layer core after the annealing and aging treatment. The area fraction of the discrete borides in the layer core was 4.6 ± 1.6%. It is understood

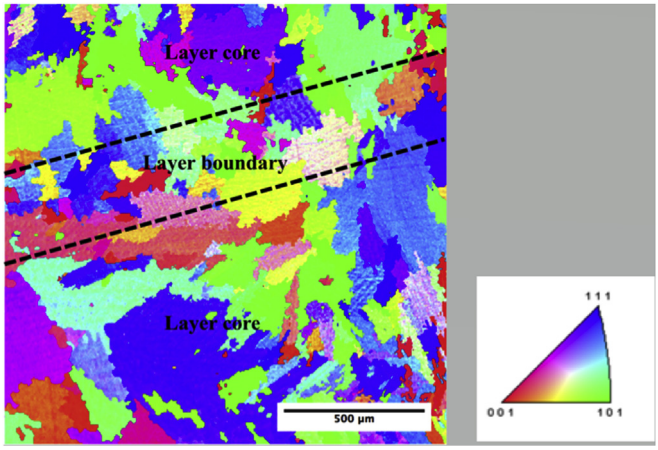

Fig. 6. EBSD map of the aged condition (with colored orientation image map in the right) showing coarsened equiaxed grains in the layer boundary and partial recrystallization in the layer core.

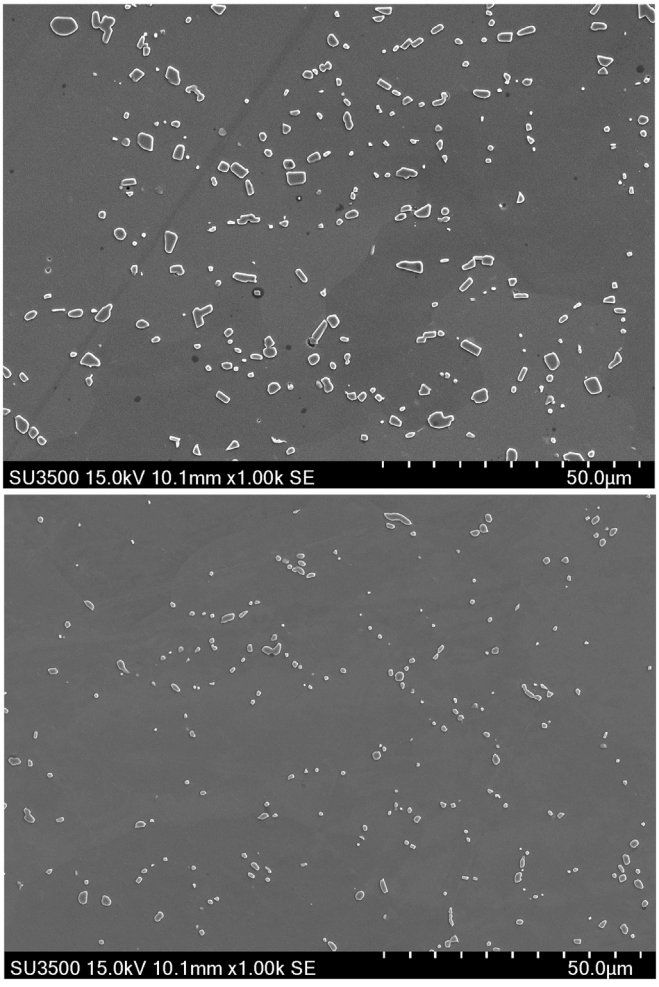

Fig. 7. (a). SEM micrograph of the layer core showing discrete borides after annealing and aging treatment; (b) SEM micrograph of the layer boundary showing smaller discrete borides precipitates than the layer core in the same annealed and aged condition.

that the annealing temperature (1205 °C) was higher than the melting temperature of the Laves phase (1191.5 °C). This led to the re-melting of the Laves phase, which corresponds to the observed microstructure. Consequently, no clear dendritic structures can be observed in the annealed and aged condition (as shown in Fig. 7(a)). As shown in Fig. 7(b), the size and area fraction of the discrete borides formed in the layer boundary are lower than in the layer core with sizes between 0.1 and 2 μm and 1.9 ± 0.8% respectively. This is attributed to similar reasons as for the aged condition: the elemental diffusion path in the layer boundary is longer than that of the layer core. It is noteworthy that the size of the discrete borides formed in the current case are lower than the gas tungsten arc deposition where, under the same conditions, were 2–15 μm in size [15]. This is correlated with the refined solidification microstructure caused by the higher cooling rates during laser wire deposition than the gas tungsten arc deposition.

EDS maps of the major alloying elements (Ni, Mo, Nb, Cr and B) were acquired to observe the elemental constitution of the different phases in the layer core of the annealed and aged condition. The results are presented in Fig. 8. As depicted, the γ matrix is

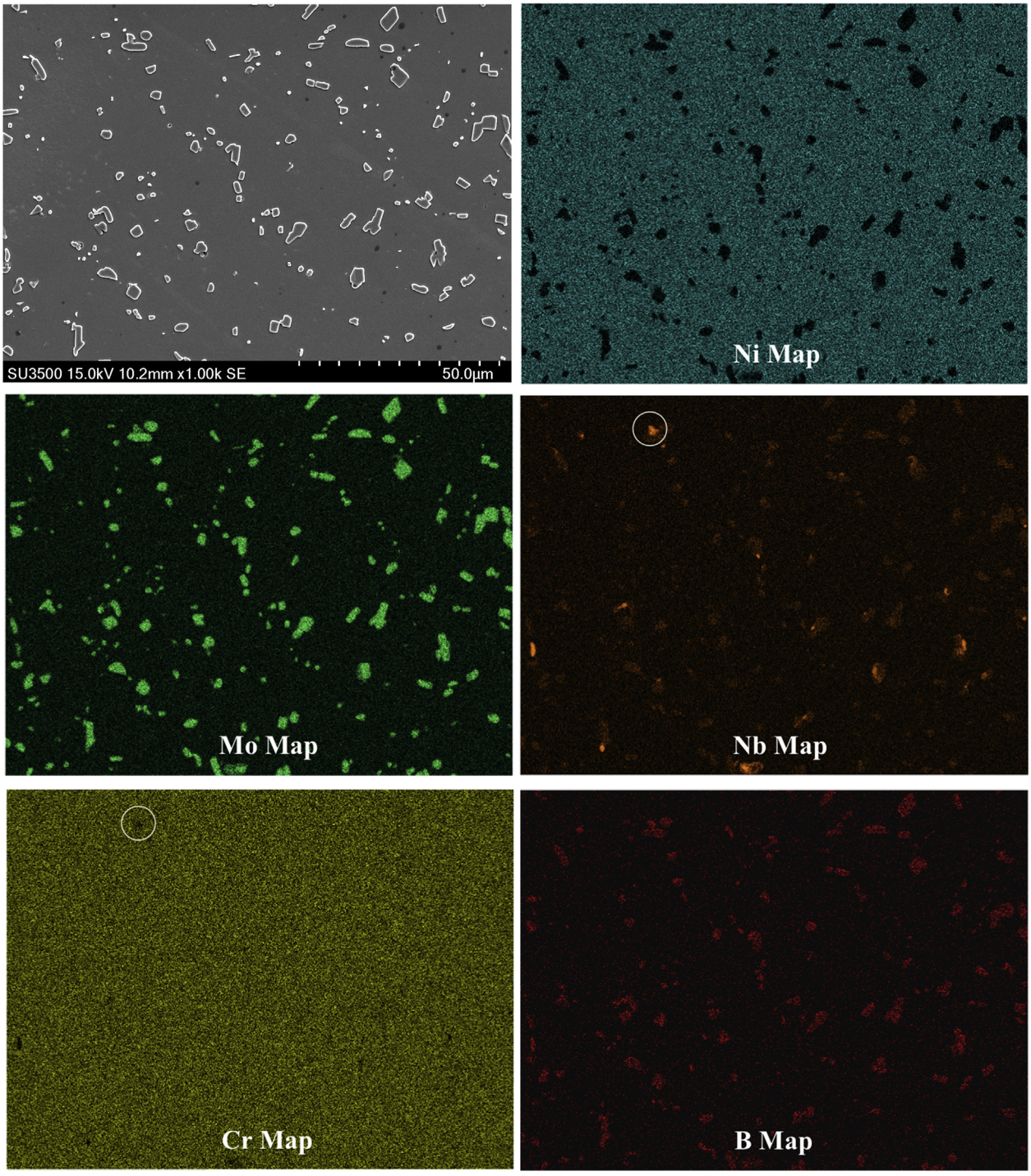

Fig. 8. (a) SEM micrograph in the layer core showing the formation of discrete borides after annealing and aging treatment; EDS maps of (b) Ni map; (c) Mo map; (d) Nb map; (e) Cr map; (f) B map. White circle represents NbC that composed of Nb and Mo, and depleted in Cr.

rich in Ni and Cr. The discrete borides are mainly composed of Mo, Cr and B. This type of (Mo, Cr) rich borides form due to the re-melting of Laves phase in 625B during high temperature heat treatment and was previously confirmed to be M_5B_3 type of boride [15]. The NbC (see circle in Fig. 8(c) and (d)) were enriched in Mo and Nb, and absent of Cr and Ni. As shown from the comparison between Figs. 2 and 8, the NbC are larger in size in the annealed and aged condition than the as-deposited condition, which is attributed to the coarsening effect during annealing and aging treatment. The EDS maps in the layer boundary after annealing and aging treatment were similar to the layer core, where discrete M_5B_3 and a few NbC were observed.

As discussed above, the annealing temperature used was higher than the re-melting temperature of the Laves phase. Due to this re-melting process it led to the disappearance of the low melting point constituents existing in the as-deposited and aged conditions. The annealing time of two hours was sufficient to re-melt all of the Laves phase, leading to the formation of coarsened isolated M_5B_3 borides during re-solidification. When the repairing of γ' nickel based superalloys is considered, the re-melting of Laves phase to produce large amounts of liquid to backfill the potential strain-age cracks formed during the heat treatment is advantageous [17].

EBSD mapping was performed to observe the grain morphology development in the annealed and aged condition, and the results are shown in Fig. 9. As depicted, the grain size in both the layer boundary and layer core after annealing and aging treatment was larger than that of the aged condition, as shown by the comparison between Figs. 6 and 9. This is due to the grain growth which occurs during the additional annealing procedure. The layer boundary is mainly constituted of equiaxed grains. In the layer core, the mixture of equiaxed grains and columnar grains can be observed, which is similar to the aged condition. Suggesting that the annealing temperature of 1205 °C was not high enough to enable a full recrystallization. Dinda et al. [25] studied the thermal stability of Alloy 625 made by laser powder deposition. They found that the columnar grains formed during deposition were partially and fully recrystallized after heat treatment of 1 h at 1100 °C and 1200 °C, respectively. However, as shown in Figs. 6 and 9, the columnar grains in the layer core developed during laser wire deposition were only partially recrystallized after both heat treatments at 1120 °C and 1205 °C. It is postulated that main reason for the difference in results obtained is due to the influence of different secondary phases. In additive manufactured conventional Alloy 625, the γ'' precipitates and δ phase are usually formed when the heat treatment temperature is higher than the re-melting temperature of Laves phase [25,29–32]. However, in the current case for 625B, the M_5B_3 borides and NbC were formed after the annealing and aging treatment, resulting in the increased recrystallization temperature.

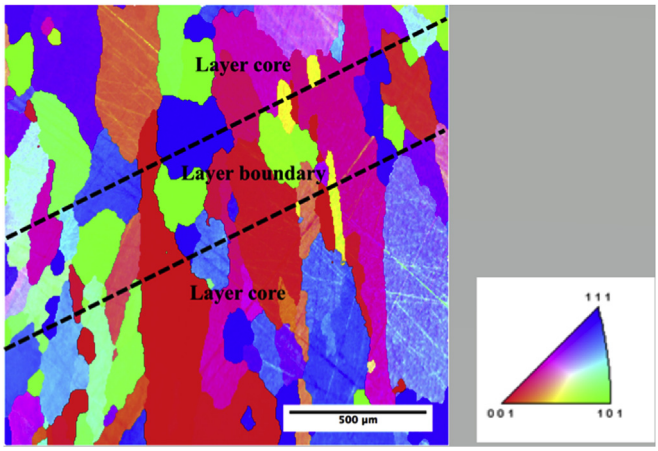

Fig. 9. EBSD map of the annealed and aged condition (with colored orientation image map inserting in the right) showing coarsened equiaxed grains in the layer boundary and partial recrystallization in the layer core.

3.4. Microhardness of the three conditions

The microhardness values of the as-deposited condition, the two-step aged condition, and the annealed and aged condition were measured to be 316 ± 14, 274 ± 12 and 288 ± 12 HV respectively. In the as-deposited condition, the hardness is mainly controlled by the continuous eutectics in the inter-dendritic regions. These eutectic features became non-continuous in the aged condition due to the Oswald Ripening of the Laves phase. This resulted in a lower hardness in the aged condition than the as-deposited condition. In the annealed and aged condition, however, the hardness is dominated by the M_5B_3 borides and small amount of NbC precipitates. These two types of secondary phases could provide a secondary phase strengthening mechanism. Nevertheless, the hardness of the annealed and aged condition is lower than the as-deposited condition owing to the coarsened size of M_5B_3 and NbC. It was reported that the hardness of laser powder deposited Alloy 625 reduced from about 260 HV in the as-deposited condition to about 190 HV after heat treatment at 1200 °C for 1 h [25]. Consequently, the hardness of all the presented conditions was superior to the conventional Alloy 625 in similar conditions.

4. Conclusion

In the current research, the influence of heat treatments on microstructure evolution and grain morphology of 625B produced via laser wire deposition was investigated. The main findings can be summarized as follows:

1. In the as-deposited condition, about 8% area fraction of eutectics was observed. This is sufficient to backfill the potential hot cracks formed during the deposition process.
2. In the as-deposited condition, continuous eutectics were observed in the inter-dendritic regions in both the layer boundary and the layer core. The eutectics include Laves phase and a small portion of NbC precipitates. The solidification features in the layer boundary were larger than the layer core due to recalescence phenomena. The non-epitaxial grain growth mode was seen, with the layer boundary being filled with small equiaxed grains, and the layer core with predominantly columnar grains.
3. After a two-step aging treatment, most of the eutectics were dissolved in the layer boundary, attributed to the longer elemental diffusion path present. Grain growth and partial recrystallization occurred during the aging treatment leading to the formation of equiaxed grains in the layer core.
4. In the annealed and aged condition, Laves phase re-melted to form discrete M_5B_3 borides. This microstructure evolution eliminated the potential strain-age cracking problems associated with the reprocessing of these alloys. This was due to the large volume of liquid formed during heat treatment from the re-melting of the eutectics. The size and area fraction of borides in the layer boundary were smaller than the layer core. Partial recrystallization was observed in the layer core, proving that the annealing temperature was still lower than the fully recrystallized temperature.

5. The microhardness of the as-deposited condition was higher than both the aged condition and the annealed and aged condition, owing to the continuous feature of eutectics in the as-deposited condition.

Acknowledgement

The authors would like to thank the financial support from NSERC through the CRD-331023745 awarded grant. The authors would also like to thank McGill Engineering Doctoral Award (MEDA) granted to Mr. Tian.

References

[1] J.N. DuPont, J.C. Lippold, S.D. Kiser, in: Welding Metallurgy and Weldability of Nickel-base Alloys, Wiley, Hoboken, N.J., 2009.
[2] M.J. Cieslak, The welding and solidification metallurgy of Alloy 625, Weld. J. 70 (1991) 49s–56s.
[3] J.J. Valencia, J. Spirko, R. Schmees, in: E.A. Loria (Ed.), Superalloys 718, 625, 706 and Various Derivates, TMS, Warrendale, PA, 1997, pp. 753–762.
[4] A. Ascari, A. Fortunato, A.H.A. Lutey, G. Guerrini, N. Pagano, Long pulse laser wire deposition of hard steels, Phy. Procedia 83 (2016) 723–732.
[5] E. Pavithra, V.S. Senthil Kumar, Microstructural evolution of hydroformed Inconel 625 bellows, J. Alloys Compd. 669 (2016) 199–204.
[6] L. Thivillon, P. Bertrand, B. Laget, I. Smurov, Potential of direct metal deposition technology for manufacturing thick functionally graded coatings and parts for reactors components, J. Nucl. Mater. 385 (2009) 236–241.
[7] A. Theriault, L. Xue, J.R. Dryden, Fatigue behavior of laser consolidated IN-625 at room and elevated temperatures, Mater. Sci. Eng.A 516 (2009) 217–225.
[8] K.H. Song, K. Nakata, Effect of precipitation on post-heat-treated Inconel 625 alloy after friction stir welding, Mater. Des. 31 (2010) 2942–2947.
[9] P. Ganesh, R. Kaul, C.P. Paul, P. Tiwari, S.K. Rai, R.C. Prasad, L.M. Kukreja, Fatigue and fracture toughness characteristics of laser rapid manufactured Inconel 625 structures, Mater. Sci. Eng. A 527 (2010) 7490–7497.
[10] X. Xing, X. Di, B. Wang, The effect of post-weld heat treatment temperature on the microstructure of Inconel 625 deposited metal, J. Alloys Compd. 593 (2014) 110–116.
[11] K. Banerjee, N.L. Richards, M.C. Chaturvedi, Effect of filler alloys on heat-affected zone cracking in preweld heat-treated IN-738 LC gas-tungsten-arc welds, Metall. Mater. Trans. A 36 (2005) 1881–1890.
[12] D. Liu, J. Lippold, J. Li, S. Rohklin, J. Vollbrecht, R. Grylls, Laser engineered net shape (LENS) technology for the repair of Ni-Base superalloy turbine components, Metall. Mater. Trans. A 45 (2014) 4454–4469.
[13] B. Alexandrov, A. Hope, J. Sowards, J. Lippold, S. McCracken, Weldability Studies of High-Cr, Ni-Base filler metals for power generation applications, Weld. World 55 (2011) 65–76.
[14] Y. Tian, B. Ouyang, A. Gontcharov, R. Gauvin, P. Lowden, M. Brochu, Microstructure evolution of Inconel 625 with 0.4 wt% boron modification during gas tungsten arc deposition, J. Alloys Compd. 694 (2017) 429–438.
[15] Y. Tian, A. Gontcharov, R. Gauvin, P. Lowden, M. Brochu, Effect of heat treatment on microstructure evolution and mechanical properties of Inconel 625 with 0.4 wt% boron modification fabricated by gas tungsten arc deposition, Mater. Sci. Eng. A 684 (2017) 275–283.
[16] J.N. DuPont, Solidification of an alloy 625 weld overlay, Metall. Mater. Trans. A 27 (1996) 3612–3620.
[17] Y. Tian, A. Gontcharov, R. Gauvin, P. Lowden, M. Brochu, Effect of heat treatments on microstructure evolution and mechanical properties of blended nickel-based superalloys powders fabricated by laser powder deposition, Mater. Sci. Eng. A 674 (2016) 646–657.
[18] A.B. Goncharov, J. Liburdi, P. Lowden, Self-healing fusion welding technology, in: Proceedings of ASME Turbo Expo 2014: Turbine Technical Conference and Exposition, 2014.
[19] A.B. Goncharov, J. Liburdi, P. Lowden, A Ductile Boron Bearing Nickel Based Welding Material, Pending Patent Application PCT/CA2014/000752, (2014).
[20] Y. Tian, R. Gauvin, M. Brochu, Microstructure evolution and rapid solidification behavior of blended nickel-based superalloy powders fabricated by laser powder deposition, Metall. Mater. Trans. A 47 (2016) 3771–3780.
[21] C.A. Schneider, W.S. Rasband, K.W. Eliceiri, Nat. Methods 9 (2012) 671–675.
[22] ASTM E112, Standard Test Methods for Determining Average Grain Size, 2014. Edition.
[23] D. Drouin, A.R. Couture, D. Joly, X. Tastet, V. Aimez, R. Gauvin, CASINO V2.42—a fast and easy-to-use modeling tool for scanning electron microscopy and Microanalysis users, Scanning 29 (2007) 92–101.
[24] Y. Tian, D. McAllister, H. Colijn, M. Mills, D. Farson, M. Nordin, S. Babu, Rationalization of microstructure heterogeneity in INCONEL 718 builds made by the direct laser additive manufacturing process, Metall. Mater. Trans. 45 (2014) 4470–4483.
[25] G.P. Dinda, A.K. Dasgupta, J. Mazumder, Laser aided direct metal deposition of Inconel 625 superalloy: microstructural evolution and thermal stability, Mater. Sci. Eng. A 509 (2009) 98–104.
[26] S. Li, Q. Wei, Y. Shi, Z. Zhu, D. Zhang, Microstructure characteristics of inconel 625 superalloy manufactured by selective laser melting, J. Mater. Sci. Technol. 31 (9) (2015) 946–952.
[27] C.V. Thompson, F. Spaepen, Homogeneous crystal nucleation in binary metallic melts, Acta Metall. 31 (1983) 2021–2027.
[28] B.S. Murty, S.A. Kori, M. Chakraborty, Grain refinement of aluminium and its alloys by heterogeneous nucleation and alloying, Int. Mater. Rev. 47 (2002) 3–29.
[29] F. Xu, Y. Lv, Y. Liu, B. Xu, P. He, Effect of heat treatment on microstructure and mechanical properties of inconel 625 alloy fabricated by pulsed plasma arc deposition, Physics Procedia 50 (2013) 48–54.
[30] L.E. Murr, E. Martinez, S.M. Gaytan, D.A. Ramirez, B.I. Machado, P.W. Shindo, J.L. Martinez, F. Medina, J. Wooten, D. Ciscel, U. Ackelid, R.B. Wicker, Microstructural architecture, microstructures, and mechanical properties for a nickel-base superalloy fabricated by electron beam melting, Metall. Mater. Trans. A 42 (2011) 3491–3508.
[31] X. Xing, X. Di, B. Wang, The effect of post-weld heat treatment temperature on the microstructure of Inconel 625 deposited metal, J. Alloys Compd. 593 (2014) 110–116.
[32] S. Li, Q. Wei, Y. Shi, Z. Zhu, D. Zhang, Microstructure characteristics of inconel 625 superalloy manufactured by selective laser melting, J. Mater. Sci. Technol. 31 (2015) 946–952.